Position Deviation Evaluation for UAV Inspecting Overhead Transmission Line Based on Measured Electric Field

Dongping Xiao, Qi Zheng, Jie Lei, and Sheng Liu

State Key Laboratory of Power Transmission Equipment & System Security and New Technology
Chongqing University, Chongqing, 400044, China
xiaodongping@cqu.edu.cn, 20161113031t@cqu.edu.cn, 201811021001@cqu.edu.cn, 20153394@cqu.edu.cn

Abstract ─ Unmanned aerial vehicle (UAV) used in overhead transmission lines (OTLs) inspection are required to fly along a preset path to conduct special tasks. However, UAVs sometimes deviate from the preset path due to positioning error or control error in practice, thereby reducing the quality of the inspection task or even leading to serious line collision accidents. In this study, a method is proposed to evaluate the UAV position deviation from the preset path in real time on the basis of a measurement and analysis on the electric field generated by transmission lines. A new idea is presented to solve the obstacle avoidance problem for UAV in transmission line inspection. To improve evaluation accuracy, the influences of transmission tower and UAV body are considered in the theoretical calculation model for electric field, and the electric field data are preprocessed to diminish the influence of environmental noise and measurement inherent error. To improve the real-time performance of the evaluation algorithm, the dynamic programming and hidden Markov model (HMM) are combined to form a dynamic-hidden Markov model algorithm, in which the parameters of the HMM are determined by the expected maximization parameter estimation and corrected in real time. The feasibility and accuracy of the proposed method are verified by several simulation examples and experiments.

Index Terms ─ Dynamic-hidden Markov model, flight deviation, transmission line inspection, unmanned aerial vehicle (UAV).

I. INTRODUCTION

Using unmanned aerial vehicle (UAV) to inspect overhead transmission lines can improve work efficiency, save manpower and material resources, and overcome the constraints of geographical environment compared with traditional manual inspection. Therefore, transmission line inspection with UAV has been promoted in recent years. To achieve the patrolling objectives and avoid collision accidents, UAVs should fly along preset paths as far as possible. If flight deviates, warning should be provided, and the position should be adjusted in time.

Several methods, such as GPS [1], machine vision ranging [2], ultrasonic ranging, radar ranging [3], optical ranging [4], and artificial potential field method [5,6], are suitable for measuring the distance between the UAV and physical object. However, these methods have limited application scenario, and improving their measurement accuracy is expensive. For example, numerous signal base stations must be built to improve the precision of GPS ranging. Therefore, a convenient and effective method is necessary to evaluate if the flight positions of UAVs deviate from the preset paths.

Many studies [7,8] have reported that AC overhead transmission lines inherently generate power frequency electric fields in their surrounding space and that the electric field intensity at a space observation point is directly related to the distance between the field point and line. On this basis, the present study proposes a new idea, that is, to use the power frequency electric field of the AV overhead transmission lines as the data foundation to evaluate whether and how much the current flight position of a UAV deviates from the preset path. As the electric fields themselves are generated by transmission lines, the electric field measuring device is a single-sided structure, unlike the laser and ultrasonic ranging devices, which requires the producing and transmitting parts of the source signal and the receiving part of the reflection signal. Moreover, power frequency electric field propagates a long distance that the sensor can measure appropriately. The electric field strength is not affected by the ambient light intensity and environment temperature, which avoids the lack of visual and infrared sensing.

The primary idea of the method proposed in this study is to regard the real-time measured electric field at the UAV's positions and the theoretically calculated electric field values at the corresponding positions on the preset path as the basic data. After preprocessing the basic data, the dynamic-hidden Markov probability model (D-HMM) is introduced to evaluate the deviation and drift direction between the current position and preset path of the UAV.

To improve the evaluation accuracy, influences of the transmission tower and UAV body on the electric field are considered in the calculation model. Moreover,

the theoretically calculated and measured electric field data are preprocessed to eliminate the influence of environmental noise and inherent measurement error before taking them into D-HMM that is used to improve the real-time performance of the evaluation algorithm.

II. IMPROVED CALCULATION MODEL OF ELECTRIC FIELD AND DATA PREPROCESSING

The accuracy of evaluating the flight position deviation of UAV with the proposed method considerably depends on the accurate calculation of the space electric field generated by AC OTLs.

A. 3D electric field calculation model considering actual states of OTL

The charge simulation method (CSM) is recommended to calculate the power frequency electric field generated by AC OTLs in a large space. An improved 3D model is presented in this study to enhance the calculation accuracy.

Figure 1 shows the constituents and layout structure of OTLs with towers. The two ends of a span fixed at Tower A and Tower B can be not at the same height. The origin of coordinate O is set at the projection on the ground of the lowest point of the span. The mathematical model of the catenary conductors can be described as [9,10]:

$$z(x) = \frac{D}{\alpha}\left(\cosh\frac{\alpha x}{D} - \cosh\frac{\alpha}{2}\right) + H \left(x_A \le x \le x_B\right), \quad (1)$$

where D is the length of span, α is the horizontal stress coefficient of conductor, and H is the lower height of conductor from the ground. Then,

$$\alpha = \gamma D / \sigma_0, \quad (2)$$

where γ and σ_0 are the specific load and horizontal stress of the conductor, respectively.
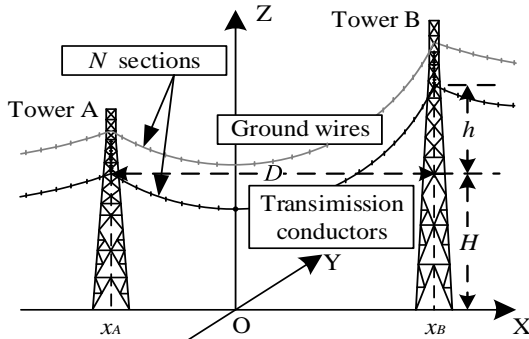

Fig. 1. Constituents and layout structure of the AC OTLs with towers.

If the height of both ends at Tower A and Tower B are equal, then $x_A = -x_B = -D/2$. Meanwhile, if the height difference between two ends is h, then,

$$\begin{cases} x_A = \frac{D}{\alpha}\text{arcsinh}\left(\frac{\alpha h}{2D}\left(\sinh\frac{\alpha}{2}\right)^{-1}\right) - \frac{D}{2} \\ x_B = \frac{D}{\alpha}\text{arcsinh}\left(\frac{\alpha h}{2D}\left(\sinh\frac{\alpha}{2}\right)^{-1}\right) + \frac{D}{2} \end{cases} \quad (3)$$

The tower comprises abundant steel bars, which will affect the electric field near them because of electromagnetic induction. A simplified model of the tower is divided into M sections [11]. In the i-th segment, the space coordinates of its head and end are (x_{i1}, y_{i1}, z_{i1}) and (x_{i2}, y_{i2}, z_{i2}), respectively. The coordinates of any point in the middle of this segment is (x_{i0}, y_{i0}, z_{i0}), as shown Fig. 2.
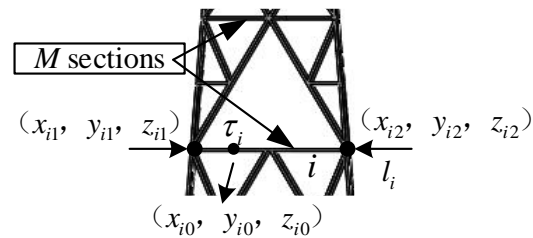

Fig. 2. Model of the tower.

A span of each overhead conductor is divided into N segments, and the coordinate setting for the endpoints of each segment is similar to that shown in Fig. 2. Then, the calculation method is unified for the overhead conductor and tower. Assuming that the length of the i-th analog line charge is l_i and the density of analog line charge is $\dot{\tau}_i$, the potential generated by the analog line charge at the spatial observation point (x, y, z) is denoted by:

$$\dot{\varphi}_i = \frac{l_i}{4\pi\varepsilon_0}\int_0^1 \dot{\tau}_i\left(\frac{1}{r} - \frac{1}{r'}\right)dt, \quad (4)$$

where ε_0 is the vacuum dielectric constant; r and r' represent the distance from the source point and its mirror point to the field point, respectively, which are denoted by:

$$\begin{cases} r = \sqrt{\Delta x^2 + \Delta y^2 + \Delta z^2} \\ r' = \sqrt{\Delta x^2 + \Delta y^2 + \Delta z'^2} \\ \Delta x = (x_{i2} - x_{i1})t + x_{i1} - x \\ \Delta y = (y_{i2} - y_{i1})t + y_{i1} - y \\ \Delta z = (z_{i2} - z_{i1})t + z_{i1} - z \\ \Delta z' = (z_{i1} - z_{i2})t - z_{i1} - z \end{cases} \quad (5)$$

where t is the normalized parameter of the distance between points (x_{i0}, y_{i0}, z_{i0}) and (x_{i1}, y_{i1}, z_{i1}), which can be shown as:

$$t = \frac{x_{i0} - x_{i1}}{x_{i2} - x_{i1}} = \frac{y_{i0} - y_{i1}}{y_{i2} - y_{i1}} = \frac{z_{i0} - z_{i1}}{z_{i2} - z_{i1}} \quad (t \in [0,1]). \quad (6)$$

The simulated charge density can be calculated after setting the known conductor potential $\varphi_{il} = U$ and tower potential $\varphi_{it} = 0$ as boundary conditions. Then, the 3D electric field components at the spatial observation point can be obtained:

$$\dot{E}_{ix} = \frac{\partial \dot{\varphi}_i}{\partial x}, E_{iy} = \frac{\partial \dot{\varphi}_i}{\partial y}, E_{iz} = \frac{\partial \dot{\varphi}_i}{\partial z} \ . \tag{7}$$

Furthermore, numerical calculations are applied to integral Equation (4) and differential Equation (7). Then, the 3D electric field components are given by:

$$\dot{E}_{ix} = \frac{\dot{\tau}_i}{2\pi\varepsilon_0} \left[\frac{a\sqrt{C} + a'\sqrt{A}}{\sqrt{C}\left(2\sqrt{AC} + B\right)} - \frac{a\sqrt{T} + (a+a')\sqrt{A}}{\sqrt{T}\left(2\sqrt{AT} + B + 2A\right)} \right]$$

$$\dot{E}_{iy} = \frac{\dot{\tau}_i}{2\pi\varepsilon_0} \left[\frac{b\sqrt{C} + b'\sqrt{A}}{\sqrt{C}\left(2\sqrt{AC} + B\right)} - \frac{b\sqrt{T} + (b+b')\sqrt{A}}{\sqrt{T}\left(2\sqrt{AT} + B + 2A\right)} \right], \tag{8}$$

$$\dot{E}_{iz} = \frac{\dot{\tau}_i}{2\pi\varepsilon_0} \left[\frac{c\sqrt{C} + c'\sqrt{A}}{\sqrt{C}\left(2\sqrt{AC} + B\right)} - \frac{c\sqrt{T} + (c+c')\sqrt{A}}{\sqrt{T}\left(2\sqrt{AT} + B + 2A\right)} \right]$$

where,

$$\begin{cases} a = x_{i2} - x_{i1} \\ b = y_{i2} - y_{i1} \\ c = z_{i2} - z_{i1} \end{cases}, \begin{cases} d = x_{i1} - x \\ e = y_{i1} - y \\ f = z_{i1} - z \end{cases}, \begin{cases} A = l_i^2 = a^2 + b^2 + c^2 \\ B = 2(ad + be + cf) \\ C = d^2 + e^2 + f^2 \\ T = A + B + C \end{cases} \ . \tag{9}$$

Finally, the 3D electric field components at the spatial observation point are superimposed the effect of all the simulated charges:

$$\dot{E}_x = \sum \dot{E}_{ix}, \dot{E}_y = \sum \dot{E}_{iy}, \dot{E}_z = \sum \dot{E}_{iz} \ . \tag{10}$$

The electric field strength can be obtained

$$E = \sqrt{\dot{E}_x^2 + \dot{E}_y^2 + \dot{E}_z^2} \ . \tag{11}$$

B. Effect of UAV on the space electric field

The shell material of the UAV used in transmission line patrol and inspection is a composite material with carbon-fiber reinforced resin matrix, which has high electrical conductivity [12,13]. Therefore, the effect of the UAV's body on the space electric field cannot be ignored.

Because the UAV body's shape is complicated and the surface potential is unknown, the electric field analysis cannot be performed with the CSM. The finite element method is suitable for solving partial differential equations on complex regions. Therefore, it is used here.

The simulation model of the UAV is built in the power frequency electric field of transmission lines, and the free tetrahedron element is used to divide the model [14,15]. The boundary conditions of the entire model are initially set. Then, the boundary potential distribution and electric field of each grid element of the UAV model can be calculated with Maxwell equations. In addition, the influence of UAV on electric field distribution can be observed by comparing the electric field distribution in the calculation domain with and without the UAV. The installation position of the electric field measurement sensor on the UAV can be determined as well. In addition, the regularity of UAV's influence also can be used to correct the measured electric field data.

C. Preprocessing of electric field data

To eliminate the influence on electric field measurement from environmental noise and the inherent error of the measuring device, the proposed evaluation method should be made suitable for OTLs with different voltage levels and arrangements. A parameter, namely, electric field ring ratio change rate K (%), is defined to preprocess the electric field data:

$$K_n = (E_{n+1} - E_n) / \max\{E_n, \ E_{n+1}\} \times 100, \tag{12}$$

where E_n is the electric field at the n-th measurement point, $n = 1, 2, 3 \ldots$. Considering the requirement of the subsequent D-HMM discriminant model, the measured and theoretical electric field data are processed similarly.

III. DEVIATION EVALUATION MODEL

By comparing the measured electric field data with the theoretical electric field data at the same observation points on the preset path, the UAV position deviation from the preset path can be judged to a certain extent. However, the actual physical conditions are difficult to simulate accurately with theoretical models, and random errors exist in the electric field measurement due to the diversity of the geographical environment and meteorological conditions. Therefore, the measured data should be further analyzed and processed, and a practical position matching algorithm with high robustness and good generalization should be studied for the UAV.

A. Background and introduction of D-HMM

The matching model based on probability can effectively overcome these problems and improve evaluation credibility. Therefore, this study uses a non-supervised probability statistical learning model based on time series data, namely, HMM [16,17]. The HMM can be used to determine the implicit parameters of the time series from the observable data sequences. Then, these parameters are used for further analyses, such as pattern recognition and fault diagnosis.

The change process of position and electric field measurement data during UAV patrol and inspection are time-series processes. Furthermore, the current position of the UAV is only related to the previous moment, which satisfies the Markov property [18]. Therefore, the position of UAV can be described by Markov chain.

The hidden here refers to the real position of the UAV, which cannot be obtained directly due to measurement error and must be inferred by the HMM model.

The electric field data are measured in real time during UAV flying. To improve the real-time performance of the model algorithm, this study combines the dynamic programming and HMM to form the D-HMM algorithm. The parameters of the D-HMM are determined with the expectation maximization parameter estimation method and corrected with the dynamic programming method in real time, where the dynamic programming algorithm is used to infer the position sequence of the UAV during flight. Figure 3 shows the main program flow chart of the D-HMM algorithm, in which the observation sequence O and EM parameter estimation and the Viterbi algorithm are three subroutines.
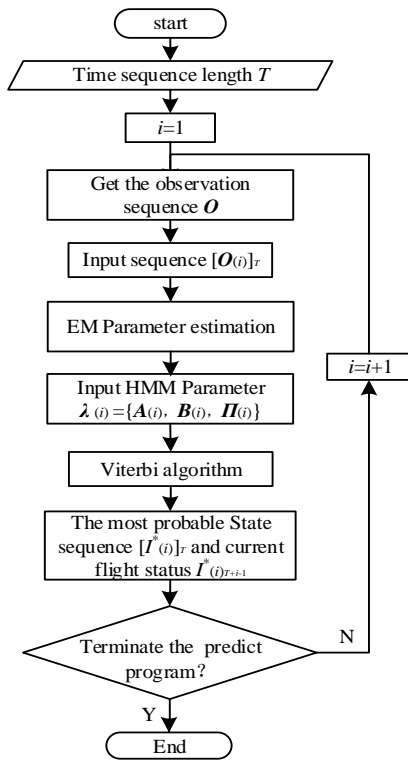

Fig. 3. Flow chart of the D-HMM algorithm.

B. Method of obtaining the observation sequence

Before running the D-HMM algorithm, to simplify the data structure of the algorithm program and improve the running speed of the program, normalizing the measured electric field data with noise is necessary.

The observation sequence $[O_{(i)}]_T$ corresponding to the measured electric field sequence is obtained by comparing the theoretical and measured electric field data after being computed and normalized, where $O_{(i)}$ represents the observation sequence of the i-th iteration.

Initially, the theoretical electric field of the eight-direction offset path around the preset path is shown in Fig. 4. Then, nine theoretical electric field sequences are obtained, where, $d = 0,1,2\cdots8$. They are converted into

theoretical K-value sequence $[K_C]_d$ following the method described in Section C of the first part. Furthermore, the time series of measured electric field is also transformed with the same method, and the time series of measured K-value $[K_M]$ is obtained. Then, the initial observation sequence $[O_{(i)}]$T is obtained by comparing sequence $[K_M]$ and sequence $[K_C]_d$ with the flight velocity v and electric field measurement time interval Δt of the UAV.
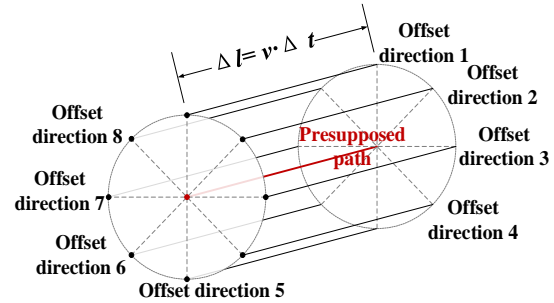

Fig. 4. Schematic of the preset path and offset direction.

C. Model training

After obtaining the input observation sequence, the model should be trained in accordance with the observation sequence to obtain the model parameters.

In practical applications, the data storage of the UAV electric field measurement is limited, the training sample capacity is small, and the data update speed is fast. To realize the rapid training of small sample statistical model, this study uses EM parameter estimation iterative algorithm to obtain HMM parameter set $\lambda = \{A, B, \Pi\}$. λ contains three types of parameters, where $A = [a_{ij}]$ is the probability transfer matrix of the real state and a_{ij} represents the probability that the real state changes from i to j. $B = [b_{ik}]$ is the probability matrix of the observed state, and b_{ik} represents the probability of the observed state being k when the real state is i. $\Pi = [\pi_i]$ is the probability vector of the initial state, and π_i represents the probability of the real state being i.

The core steps of the EM algorithm include the two parts of the problem expectation expression and the expectation maximization calculation [19]. In the proposed algorithm model, the expected Q expression is denoted by:

$$Q(\lambda_x, \lambda_{x-1}) = P(O, I \mid \lambda_{x-1}) \sum_I \log \pi_{i(t=1)}$$
$$+ P(O, I \mid \lambda_{x-1}) \sum_I \left(\sum_{t=1}^{T-1} \log a_{i(t)j(t+1)} \right) \quad . \quad (13)$$
$$+ P(O, I \mid \lambda_{x-1}) \sum_I \left(\sum_{t=1}^{T} \log b_{i(t)k(t)} \right)$$

The three elements of HMM appear in the three parts of Equation (13). Therefore, only the three parts of the Q function should be maximized to obtain the model parameters:

$$\pi_{xi} = \gamma_{(1)}(i)$$
$$a_{xij} = \sum_{t=1}^{T-1} \xi_{(t)}(i,j) / \sum_{t=1}^{T-1} \gamma_{(t)}(i) \quad , \qquad (14)$$
$$b_{xik} = \sum_{t=1, b_t=k}^{T} \gamma_{(t)}(i) / \sum_{t=1}^{T} \gamma_{(t)}(i)$$

where,

$$\gamma_{(t)}(i) = P\left(i_{(t)} \mid \mathbf{O}, \lambda_{x-1}\right)$$
$$\xi_{(t)}(i,j) = P\left(i_{(t)}, j_{(t+1)} \mid \mathbf{O}, \lambda_{x-1}\right) \qquad (15)$$

By substituting Equation (15) into Equation (14), the model parameter λ_x calculated by the x-th iteration can be obtained. For one input observation sequence $\mathbf{O}$, x iterations are performed. If λ_x converges to λ or reaches the maximum number of iterations, then λ is the output parameter of the model.

D. Dynamic update of HMM parameter

With the movement of the UAV, the track of the UAV will change constantly, and the measured electric field data will be updated constantly. To improve the real-time and accuracy of the algorithm further, the parameters of the algorithm model are continuously corrected with the updating of the input data. In this study, a parameter dynamic update module is added to the HMM algorithm to form the D-HMM algorithm.

The value of the algorithm parameter set λ is affected by the observation sequence. Hence, a well-designed dynamic update scheme of the observation sequence can simultaneously realize the dynamic update of the λ parameter.

When the algorithm runs for the first time, the observation sequence is recorded as $\mathbf{O}_{(1)}$, and the sequence length is T. When the data at time $t = T+1$ is measured, the data at time $t = 1$ is discarded to form a new observation sequence $\mathbf{O}_{(2)}$. In this manner, the real-time input sequence group of D-HMM can be obtained. Figure 5 shows the dynamic selection of the input observation sequence.
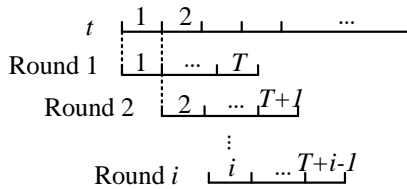
Fig. 5. Dynamic selection of the input observation sequence.

This dynamic selection method of the propulsion input sequence not only preserves the contribution of each measurement data to the calculation of the algorithm parameters during flight but also effectively reduces the sensitivity of the algorithm to the initial parameters. Moreover, this method controls the length of the input

sequence, improves the running speed of the algorithm, and enhances the accuracy and timeliness of the discriminant results.

E. Position deviation evaluation

On the basis of the model parameters, the subsequent step is to evaluate whether the UAV deviates from the preset path, particularly the direction and distance of the deviation in a continuous period of time. UAV offset measurement is essentially an optimization analysis problem for a multi-step multi-state process. In this study, the dynamic programming Viterbi algorithm is used to solve the D-HMM model of the known observation sequence $\mathbf{O}$ and parameter λ. At this time, the optimal hidden sequence corresponding to the observation sequence is obtained, that is, the true migration of UAV. The core idea of the Viterbi algorithm is that, in the multi-step and multi-choice problem, each step retains the optimal solution of the previous step and finds the optimal path of the transition between multiple steps through the backtracking method [20,21]. Figure 6 shows the algorithm flow.
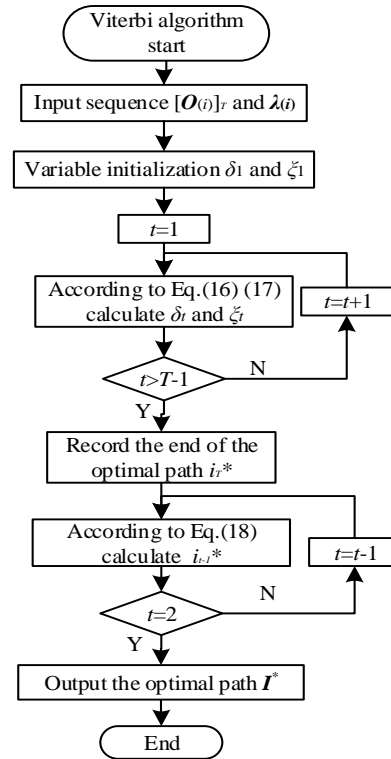
Fig. 6. Flow chart of the Viterbi algorithm.

The variable $\delta_t(i)$ represents the probability of the optimal path in all paths leading to state i at a certain time t. The variable $\Psi_t(i)$ represents the state of the optimal path starting point to state i at time t, the recursive expressions of $\delta_t(i)$ and $\Psi_t(i)$ are as follows:

$$\delta_t(i) = \max_{1 \le i, j \le 9} [\delta_{t-1}(j)a_{ji}]b_{ik(t)}, \qquad (16)$$

$$\psi_t(i) = \arg \max_{1 \le i, j \le 9} [\delta_{t-1}(j)a_{ji}]. \qquad (17)$$

By the forward recursive calculation, the probability P^* corresponding to the last node of the time series and the state I_T^* of the node are obtained. On the basis of the formula,

$$i_t^* = \psi_{t+1}(i_{t+1}^*). \qquad (18)$$

The last node is inversely backtracked to obtain the entire optimal path $I^* = [i_1^*, i_2^*, \ldots, i_T^*]$, that is, the UAV deviates from the preset path evaluation result for a period.

IV. EXAMPLE AND EXPERIMENT

To verify the feasibility and validity of the proposed method, a numerical example and experimental scheme are shown here. In the numerical example, assuming that the UAV flight control system is in perfect condition, the real flight path of the UAV coincides with the preset path, but the electric field measurement device has measurement errors. This scheme is designed to verify the effectiveness of the path discrimination algorithm in the case of limited accuracy of the airborne measuring device. The experimental conditions of the experimental verification are set as follows: set up a test site to simulate an experimental platform, set an experimental path that deviates from the preset path, measure the electric field on the path, and input the algorithm model to simulate the discriminant experiment. This scheme is close to the actual situation and aims to verify the feasibility of the algorithm.

A. Numerical verification

The preset path and offset range are set as shown in Fig. 7, and the preset path is numbered as state 0. The four offset states shown in the figure correspond to state numbers 1–4. Figure 8 shows the corresponding K values of the preset paths and offset states.

If the flight plan of UAV is to fly straight from one base tower to the next at a uniform speed, then the flight path is at a horizontal distance of 5 m from the side phase, the height is the same as the ground line suspension, and the total length of the path is 300 m. The electric field is measured every meter of flight. When the UAV reaches the end of the preset path, 301 electric field measurement data are obtained. Then, the corresponding 300 K-values can be calculated. Ideally, the flight state observation sequence of the UAV on the preset path is $O_E = [\underbrace{0, 0, 0, \ldots, 0, 0, 0}_{300^* 0}]$.

The length of the sequence selected by one calculation is set to T=10. To show the UAV flight without offset, the vector representing the probability of actual flight state should be set to $\boldsymbol{\Pi} = [1, 0, 0, 0, 0]$. The length

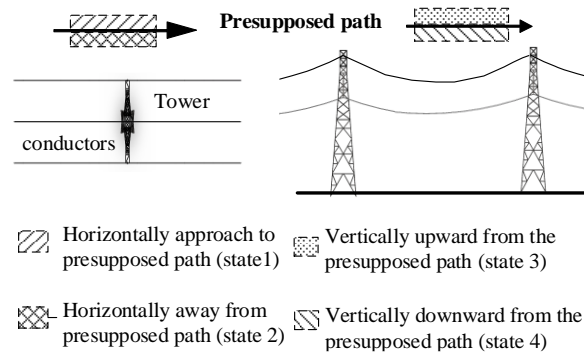of the sequence selected by one calculation is set to T=10.

Fig. 7. Schematic of the preset path and offset range (top view and left view).
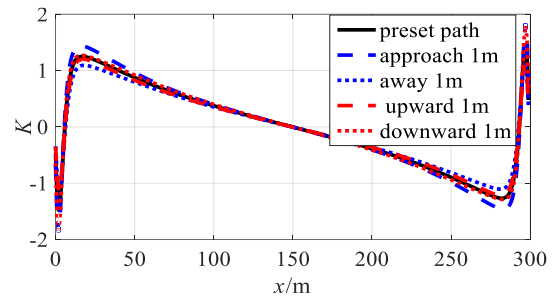

Fig. 8. Preset path and offset value corresponding to the K value.

To show the UAV flight without offset, the vector representing the probability of actual flight state should be set to $\boldsymbol{\Pi} = [1, 0, 0, 0, 0]$. The random errors of 5%, 10%, 15%, and 20% are superimposed on the electric field value of the preset path to calculate the corresponding K-value. As shown in Fig. 9, the state closest to the K-value is found and forms the observation sequence O. The path state I^* is determined by the D-HMM algorithm. Taking the first 10 m of the flight as an example, in one calculation, the measurement error is set to 5%. The input observation sequence is $O_{5\%} = [1, 2, 0, 3, 4, 1, 2, 1, 2, 1]$, and the output path state sequence is $I^*_{5\%} = [0, 0, 0, 0, 0, 0, 0, 0, 0, 0]$. Therefore, the flight state of UAV is along the preset path without offset in the course of 10 m uniform straight flight from one base tower to the next.

For each of these error ranges, discriminant calculations are performed 30 times using the algorithm model without adding a dynamic parameter update module, and 10 discriminant points are calculated each time. The discriminant error rate of the proposed algorithm is recorded in each error range. Then, the algorithm model of the dynamic parameter update module is used to discriminate the same point. Table 1 shows the results.

Table 1: Accuracy of different error range algorithms

Error Range	Discriminant Point	No Dynamic Parameter Updating Module		Dynamic Parameter Updating Module	
		Number of Errors	Error Rate	Number of Errors	Error Rate
5%	300	25	8.33%	7	2.33%
10%	300	28	9.33%	8	2.67%
15%	300	30	10%	9	3%
20%	300	33	11%	11	3.67%

The D-HMM algorithm with dynamic parameter update module effectively reduces the error rate and improves the effectiveness of the UAV offset state discrimination algorithm when a certain error exists in the electric field measurement.

B. Experimental verification

In the laboratory environment, an experimental platform is simulated. Three copper rods with length of 3 m and diameter of 1 cm are used to simulate the single-return three-phase transmission lines. Wooden supports with height of 2 m are used at both ends of each conductor. The three-phase conductors are arranged horizontally, and the phase spacing is set at 1.5 m. Three wires are connected to 1 kV three-phase transformer through lead wire. The three wires from left to right are A, B, and C phases, respectively. Figure 9 presents the schematic of the simulated experimental platform, and Fig. 10 displays the real object.
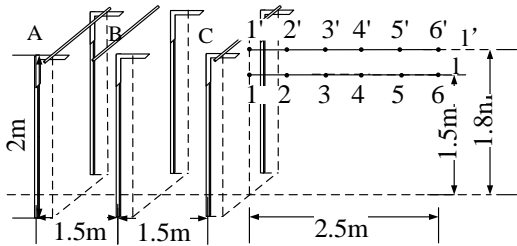

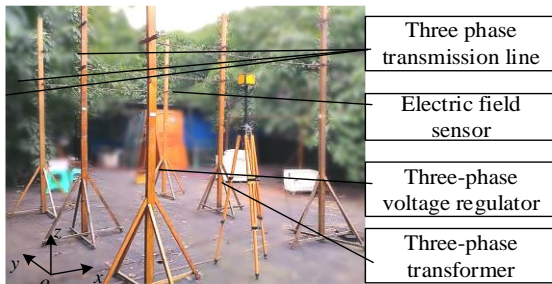Fig. 9. Schematic of the simulated experimental platform.

Fig. 10. Physical chart of the simulated experimental platform.

Starting from the midpoint of the side phase conductor, the straight-line l in Fig. 9 is set as the preset path of the UAV with a height of 1.5 m. The flight direction is 6→1. An offset straight-line l' is set directly above the straight-line l, and the height is 1.8 m. The actual flight path of UAV is set to be 6'→5'→4→3→2'→1. Table 2 shows the measured electric field, calculated K value, and discriminant results. Except for the first measurement data without output and the last point has low confidence in discrimination, the remaining points can correctly determine the path offset state. The validity of the proposed algorithm in the laboratory environment is verified.

Table 2: Experimental data and results

Sequence	Electric Field (V/m)	Value of K	Discriminant Result
1	43.9		
2	63.7	31.1	5
3	111.6	42.9	4
4	195.2	42.8	3
5	377.5	48.3	2
6	607.2	37.8	1

V. CONCLUSION

This study proposes a method to evaluate the position deviation of UAV from the preset path in real time by using electric field information. Initially, considering the influences of transmission tower and UAV body, a calculation method of spatial electric field distribution is introduced. Then, dynamic programming and HMM are combined to form the D-HMM algorithm for evaluating the deviation of UAV from the preset path. This algorithm can dynamically update model parameters and meet the real-time and accuracy requirements of the deviation evaluation when the UAV is flying with high speed. Finally, the feasibility and effectiveness of the proposed method are verified through numerical calculation and experiments. The application of electric field information in the flight control of line patrol UAV is discussed in depth. This study provides a new thinking of auxiliary UAV flight control and ensures the quality of the inspection task and avoids collision by evaluating the position deviates.

In the future, the work space of multi-functional civil UAVs, such as logistics, photography, and exploration UAVs, and transmission line corridors can have inevitable intersections. The method proposed in this study also provides a new idea for the autonomous obstacle avoidance of generally using UAV.

REFERENCES

[1] J. Kwak and Y. Sung, "Autonomous UAV flight control for GPS-based navigation," *IEEE Access*, vol. 6, pp. 37947-37955, 2018.

[2] E. Zhang and S. Wang, "Plane-space algorithm based on binocular stereo vision with its estimation of range and measurement boundary," *IEEE Access*, vol. 6, pp. 62450-62457, 2018.

[3] P. Peng, L. X. Guo, C. M. Tong, and B. Chen, "A high resolution radar range profile simulator for low flying target above sea surface with multipath effect," *2017 International Applied Computational Electromagnetics Society Symposium (ACES)*, Suzhou, pp. 1-2, 2017.

[4] N. Gageik, P. Benz, and S. Montenegro, "Obstacle detection and collision avoidance for a UAV with complementary low-cost sensors," *IEEE Access*, vol. 3, pp. 599-609, 2015.

[5] Y. Rasekhipour, et al., "A potential field-based model predictive path-planning controller for autonomous road vehicles," *IEEE Transactions on Intelligent Transportation Systems*, vol. 18, no. 5, pp. 1255-1267, May 2017.

[6] G. Wen, et al., "Artificial potential-based adaptive H∞ synchronized tracking control for accommodation vessel," *IEEE Transactions on Industrial Electronics*, vol. 64, no. 7, pp. 5640-5647, July 2017.

[7] W. Yao, et al., "Pioneer design of non-contact synchronized measurement devices using electric and magnetic field sensors," *IEEE Transactions on Smart Grid*, vol. 9, no. 6, pp. 5622-5630, Nov. 2018.

[8] C. Liao, et al., "Helicopter live-line work on 1000-kV UHV transmission lines," *IEEE Transactions on Power Delivery*, vol. 31, no. 3, pp. 982-989, June 2016.

[9] A. Z. El Dein, M. A. A. Wahab, M. M. Hamada, and T. H. Emmary, "The effects of the span configurations and conductor Sag on the electric-field distribution under overhead transmission lines," *IEEE Transactions on Power Delivery*, vol. 25, no. 4, pp. 2891-2902, Oct. 2010.

[10] D.-P. Xiao, W. He, F. Yang, Z.-L. Zhang, and J. Tang, "Power frequency electric field calculation and span selection for UHV transmission lines with different meteorological conditions," *High Voltage Eng.*, vol. 35, no. 9, pp. 2081-2086, 2009.

[11] A. Z. El Dein, "Calculation of the electric field around the tower of the overhead transmission lines," *IEEE Transactions on Power Delivery*, vol. 29, no. 2, pp. 899-907, Apr. 2014.

[12] A. Mehdipour, et al., "Advanced carbon-fiber composite materials for RFID tag antenna applications," *Applied Computational Electromagnetics Society Journal*, vol. 25, no. 3, pp. 218-229, 2010.

[13] E. C. Senis, et al., "Enhancement of the electrical and thermal properties of unidirectional carbon fibre/epoxy laminates through the addition of graphene oxide," *Journal of Materials Science*, vol. 54, no. 12, pp. 8955-8970, June 2019.

[14] A. Takei, et al., "High-accuracy electromagnetic field simulation using numerical human body models," *IEEE Transactions on Magnetics*, vol. 52, no. 3, pp. 1-4, Mar. 2016.

[15] F. Aouabed, et al., "Finite element modelling of electric field and voltage distribution on a silicone insulating surface covered with water droplets," *IEEE Transactions on Dielectrics and Electrical Insulation*, vol. 25, no. 2, pp. 413-420, Apr. 2018.

[16] N. Asadi, A. Mirzaei, and E. Haghshenas, "Creating discriminative models for time series classification and clustering by HMM ensembles," *IEEE Transactions on Cybernetics*, vol. 46, no. 12, pp. 2899-2910, Dec. 2016.

[17] H. Li, *Statistical Learning Method*, Beijing, China: Tsinghua Univ. Press, 2012.

[18] M. El Yazid Boudaren, et al., "Phasic triplet Markov chains," *IEEE Transactions on Pattern Analysis and Machine Intelligence*, vol. 36, no. 11, pp. 2310-2316, Nov. 2014.

[19] F. Guo, O. Wu, Y. Ding, and B. Huang, "A data-based augmented model identification method for linear errors-in-variables systems based on EM algorithm," *IEEE Transactions on Industrial Electronics*, vol. 64, no. 11, pp. 8657-8665, Nov. 2017.

[20] Q. Huang, et al., "Trimming soft-input soft-output Viterbi algorithms," *IEEE Transactions on Communications*, vol. 64, no. 7, pp. 2952-2960, July 2016.

[21] C. Soltanpur and J. R. Cruz, "Near optimal Viterbi algorithm for storage channels with linear regressive noise," *IEEE Journal on Selected Areas in Communications*, vol. 34, no. 9, pp. 2518-2524, Sep. 2016.

Dongping Xiao was born in Xuanwei, Yunan Province in 1977. She received the B.Sc. degree in Industrial Automation from Chongqing University, Chongqing, China, in 1999, and the M.Sc. and Ph.D. degrees in Electrical Engineering from Chongqing University, in 2004 and 2009, respectively. From 2012 to 2013, she was a Visiting Scholar with Washington State University, USA. Currently, she is an Associate Professor at the College of Electrical Engineering, Chongqing University, China. Her main fields of interests include calculation and simulation of electromagnetic field, electromagnetic measurement and running state monitoring of power transmission equipment.